Mechanically-Robust Electrospun Nanocomposite Fiber Membranes for Oil and Water Separation

Marat Nueraji,[a] Zhexenbek Toktarbay,[b] Aida Ardakkyzy,[c] Deepak Sridhar,[d,e] Hassan Algadi,[f] Ben Bin Xu,[g] Jalal T. Althakafy,[h] Abdullah K. Alanazi,[i] Hala M. Abo-Dief,[j] Salimgerey Adilov,[c,] and Zhanhu Guo[d,g*]*

[a] Edward R. Murrow High School, Brooklyn, NY 11230, USA.
[b] Renewable Energy Systems and Material Science Laboratory, National Laboratory Astana (NLA), Nazarbayev University, Kabanbay Batyr 53, Astana,010000, Kazakhstan.
[c]Department of Chemistry, School of Science and Humanities, Nazarbayev University, Kabanbay Batyr 53, Astana,010000, Kazakhstan.
[d] Integrated Composites Lab (ICL), Department of Chemical and Biological Engineering, University of Tennessee, Knoxville, TN, USA
[e] Zentek Ltd. 24 Corporate Crt, Guelph, Ontario, N1G 5G5 Canada
[f] Department of Electrical Engineering, Faculty of Engineering, Najran University, Najran, 11001, Saudi Arabia
[g] Mechanical and Construction Engineering, Faculty of Engineering and Environment, Northumbria University, Newcastle Upon Tyne, NE1 8ST, UK
h Department of Chemistry, Faculty of Applied Science, Umm Al-Qura University, Makkah 24230, Saudi Arabia
i Department of Chemistry, College of Science, Taif University, P.O. Box 11099, Taif 21944, Saudi Arabia
[j] Department of Science and Technology, University College-Ranyah, Taif University, P.O. Box 11099, Taif 21944, Saudi Arabia

**: sadilov@nu.edu.kz (S. Adilov); or zhanhu.guo@northumbria.ac,uk (Z. Guo)*

Abstract

Mechanically-robust nanocomposite membranes have been developed via crosslinking chemistry and electrospinning technique based on the rational selection of dispersed phase materials with high Young's modulus (i.e., graphene and multiwalled carbon nanotubes) and Cassie-Baxter design and used for oil and water separation. Proper selection of dispersed phase materials can enhance the stiffness of nanocomposite fiber membranes while their length has to be larger than their critical length. Chemical modification of the dispersed phase materials with fluorochemcials and their induced roughness were critical to achieve superhydrophobocity. Surface analytic tools including goniometer, X-ray photoelectron spectroscopy (XPS), Fourier transform infrared (FTIR) spectroscopy, Raman spectroscopy, atomic force microscopy (AFM) and scanning electron microscope (SEM) were applied to characterize the superhydrophobic nanocomposite membranes. An AFM-based nanoindentation technique was used to measure quantitativly the stiffness of the nanocomposite membranes for local region and whole composites, compared with the results by a tensile test technique. Thermogravimetric analysis (TGA) and differential scanning calorimetry

(DSC) techniques were used to confirm composition and formation of nanocomposite membranes. These membranes demonstrated excellent oil/water separation. This work has potential application in the field of water purification and remediation.

Keyword: Oil; Separation; Membrane; Electrospinning; Polymer nanocomposites.

1. Introduction

Sea oil exploration, extraction, and transportation increase the risk of oil spills into the water. In recent years, incidents of oil spills, especially deep sea oil leaks, can be seen more frequently in different locations of the world (Beyer et al., 2016; Cirer-Costa, 2015; Nelson et al., 2018; Wiley, 2013). According to the International Tanker Owners Pollution Federation Limited (ITOPF) (International Tanker Owners Pollution Federation, London, UK, 2010), a significant number of oil spill cases at different magnitudes took plance between 1970 and 2020. Among them, 1381 cases had over 7000 tons of oil spilled into the ocean and 466 of these cases had between 7 and 7000 tons of oil spilled. Three incidences of oil spills that leaked between 7 and 7000 tons of oil into the ocean occurred in 2020 alone [ITOPF] (International Tanker Owners Pollution Federation, London, UK, 2010). The pollutions from natural oil leakage and industrial waste have harmed the seafood industry from both environmental and economic aspects (de Oliveira Estevo et al., 2021) and the financial cost to purify and restore water is still expensive (Egan et al., 2021). On the reverse side, the presence of water impurity in diesel fuel, gasoline fuel and even crude oil not only damages car engines but also causes a multitude of safety risks to petroleum refinery. The contaminated fuel slows the combustion process, which increases hydrocarbon emission and causes corrosion in the engine (Peters and Stebar, 1976; Singh et al., 2020). Furthermore, the water impurity in the fuel increases the freezing point, which leads to a decrease in engine efficiency (Ritchie and Kulawic, 1970).

Currently, the purification of oil or water from one another is still a challenge. Although a number of technologies have been developed, the membrane-based technology has drawn broad attention due to its low cost, easy process-ability, and reusability. Recently, superhydrophobic membranes have been successfully used for the separation of oil and water (Hong et al., 2018; Huang et al., 2013; Lei et al., 2017; Zeiger et al., 2017). Polystyrene (PS) is one of the materials, which can be used to produce the membrane with the merit of its low cost and excellent resistance in any harsh media. However, its low mechanical property hampers the application in the membrane technology. Developing composites might be a potential solution for the problem. Stiffness of the bulk materials can be enhanced by adding small amount of the materials with high Young's modulus. On the other hand, proper selection and optimal design between dispersed phase materials and matrixes are still challenges. Furthermore, since carbon nanotubes (CNTs) exhibit outstanding mechanical properties such as high stiffness and high flexibility, inclusion of CNTs in the membrane might address the mechanical weakness of the membrane (Rodrigues et al., 2016). But, inertness of the CNT is a major obstacle for fabricating composites with polymers. For this, carboxylation and hydroxylation of CNTs by oxidation reaction improve the reactivity of CNT toward complexation with other materials, thus facilitating the fabrication process (Datsyuk et al., 2008). The carboxyl and hydroxyl groups of CNTs further reacted to produce the composite membrane through the silanization reaction (Ihsanullah, 2019; Wu et al., 2019).

Superhydrophobic surfaces are well-known for repelling water (Nuraje et al., 2013). These surfaces can be obtained via optimizing surface roughness of the membrane and adding various sizes of nanoparticles (Asmatulu et al., 2011; Sun et al., 2017). Our team and other groups also developed super-hydrophobic polymeric nanofibers (Kang et al., 2008; Nuraje et al., 2013). However, the composite membranes especially the comparison of fillers of CNTs and graphene have not been reported for oil-water separation.

In this study, the electrospinning technique was used to produce superhydrophobic polymeric composite membranes via controlling nano and microsize porous structures of fibres. This work aims to develop superhydrophobic PS composite membranes with strong mechanical properties for the separation of oil and water based on two strategies. The first strategy is that the superhydrophobicity improves oil separation from the mixture of oil and water. The second strategy is to enhance robustness of the PS membrane via rationally designing composites. This work will study two types of electrospun nanocomposite membranes for oil water separation. One is the PS nanocomposite membranes with modified MWCNT, and the other one is the PS nanocomposite membranes with graphene. Their mechanical and surface properties will be studied in details for oil water separation efficiency.

2. Experimental

2.1 Materials

Multiwall carbon nanotube (MWCNT), 1H,1H,2H,2H perflurodecyltriethoxysilane, polystyrene (PS), H_2SO_4:HNO_3, and dimethylformamide (DMF) were purchased from Sigma-Aldrich.

2.2 Fabrication of polystyrene nanocomposite membrane

Polystyrene nanocomposite membranes were fabricated in three steps: generation of functional groups, silanization of CNT or graphene, and production of electrospun composite. The details are stated as follows:

Functionalization (oxidation) of MWCNTs

In the first step, the acid treatment approach was applied to generate functional groups on the surface of MWCNT or graphene using a mixture of concentrated H_2SO_4:HNO_3 at 3:1 (v/v). To summarize, first, 0.1 g of MWCNT was dispersed in a mixture of concentrated H_2SO_4:HNO_3 3:1 (v/v). Then, the reaction was stirred for 20 hours at 50ºC. Finally, the mixture was washed with fresh distilled water until the pH value reaches 6 – 6.5.

Silanization of Multiwalled Carbon Nanotubes (MWCNT) with alkyl fluorosilane:

In this step, two different alkyl silane molecules were applied to modify MWCNT or graphene. In brief, silanization reaction of MWCNT with alkyl fluorosilane was carried out in toluene solution. 1H,1H,2H,2H perflurodecyltriethoxysilane was used as alkyl fluorosilane. The above functionalized MWCNT (0.017 g) was added into a flask containing 1H,1H,2H,2H perflurodecyltriethoxysilane (2 mL) at 1:1 mole ratio and heated to 80ºC for 20 hours. Finally, the modified MWCNT was removed from the solution by centrifugation, washed with fresh acetone and water, and dried in vacuum oven. **Figure 1** shows the reaction between functionalized MWCNT and 1H,1H,2H,2H perflurodecyltriethoxysilane.

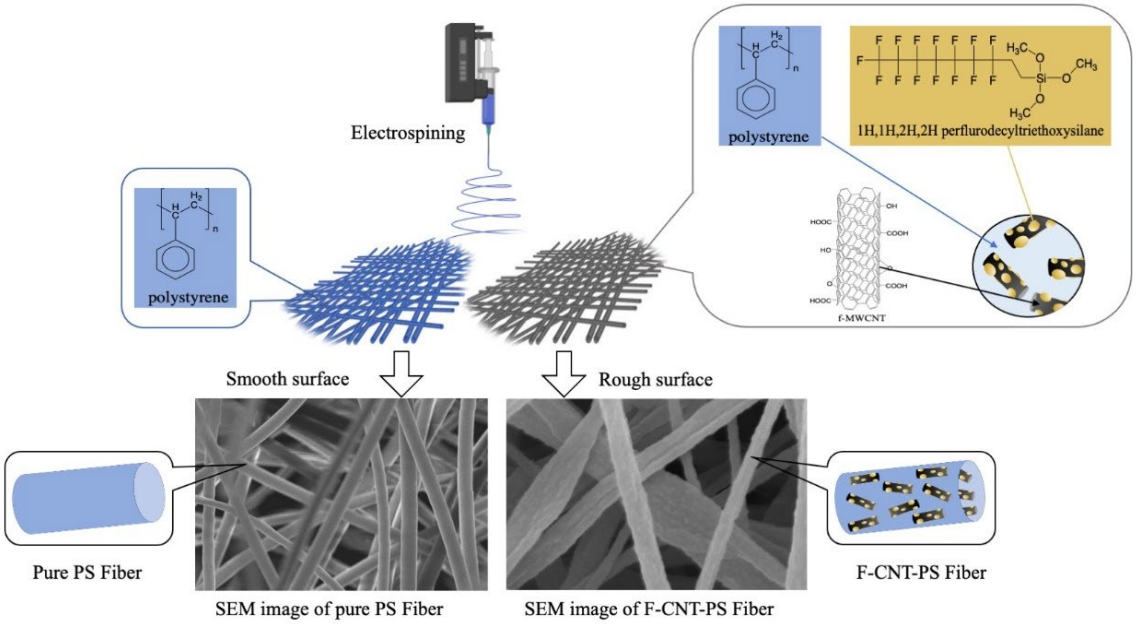

Figure 1. Schematic Illustration of the Formation Mechanism of the Superhydrophobic Structure by Electrospinning of Polymer Solutions with MWCNT modified with 1H,1H,2H,2H perflurodecyltriethoxysilane. F-CNT indicates functionalized MWCNT with modified with 1H,1H,2H,2H perflurodecyltriethoxysilane.

Electrospinning of polystyrene solution of silanized MWCNT.

First, 0.03 g of the silanized MWCNT sample from the above reaction was added to 3 mL of 20 % PS in dimethylformamide (DMF) solvent and sonicated for 30 min. Then, the solution was stirred for 5 more hours to obtain fully dispersed silanized MWCNT into the PS. Next, the mixture was poured into a syringe with a needle diameter of 0.9 mm for electrospinning, which was fixed on the electrospinning machine. The electrospinning parameters were used as follows: pumping rate at 1.2 mL/h, and the distance from the needle to the surface of 17 cm. The applied positive voltage was 15 kV and a negative voltage of -5 kV was applied to the receiver, which was aluminum foil. The final product was labelled as PS-MWCNT-SiF.

The fabrication of polystyrene and graphene nanocomposite fibres followed the above described fabrication procedures of polysytrene and MWCNT nanocomposite fibers to produce the polystyrene-graphene nanocomposite fibers, which are labelled as PS-G-SiF.

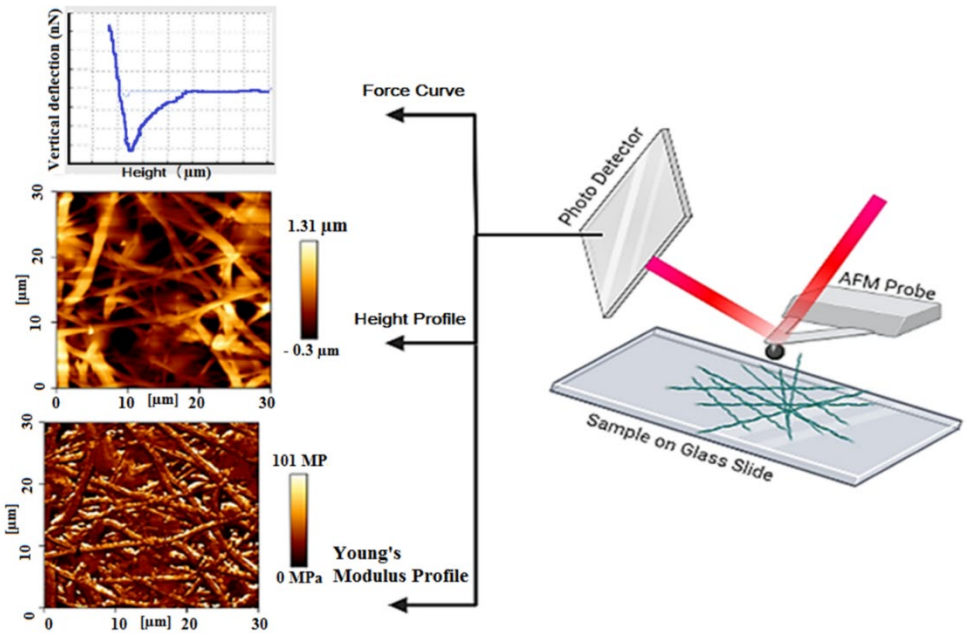

Figure 2. (Right) Schematic description of AFM working for determination of Young's modulus of composite fibers. (Left Top) A curve of forces and height was recorded through detector. (Left middle) Topological image obtained by AFM and (left bottom) Young's modulus was obtained by applying Hertz model.

2.3 Characterization

Scanning electron microscopy (SEM, Crossbeam 540) and atomic force microscopy (AFM, NanoWizard III) were applied to obtain the topological information of the nanofibers.

Raman spectroscopy (The Horiba LabRam Evolution, Japan) and FTIR spectroscopy (ANicolet iS10) in combination with XPS analyses (NEXSA, Thermo Scientific) were utilized to confirm the chemical modification of MWCNT and graphene. The compositions of the composite materials and their phase diagram were obtained by using both thermogravimetric analysis (TGA) and differential scanning calorimetry (DSC) technique. Thermal analysis carried out with a Thermal Analyzer (STA) 6000 in Nitrogen environment, heated from 30.00°C to 800.00°C at 10.00°C/min. Contact angles of the membranes were determined by a goniometer (Dataphysics OCA 15Pro).

2.4 Mechanical property of composite membranes

Measurement of stiffness by AFM: The atomic force microscope (AFM, NanoWizard III, JPK Instruments) was used to measure the height and Young's modulus of fibers. The AFM offers a 100 µm x 100 µm lateral and 15 um vertical range of scanning with various imaging modes. The basic principle to obtain different profiles is illustrated in **Figure 2 and Figure S1**.

A texture analyzer machine (Stable Micro Systems, UK) was applied to obtain the mechanical properties of the composite fibers. The samples were cut into rectangular shapes of 1 cm in width and 4 cm in length. After that, samples were clamped at both ends on the tensile machine and pulled at 1 mm/sec. The Young's modulus of polymer composite fibers was determined by stress-strain curve.

2.5 Oil/water separation experiment.

In the oil and water separation experiment, either PS-G-SiF or PS-MWCNT-SiF composite membrane was shaped into a cylinder with a diameter of 3.5 cm and thickness of 0.15 mm. Then, the top of the membrane was placed onto the separation funnel. The mixture of water, cyclohexane, and chloroform was poured to measure the separation value of the membrane. The separation process was carried out by the gravitational force.

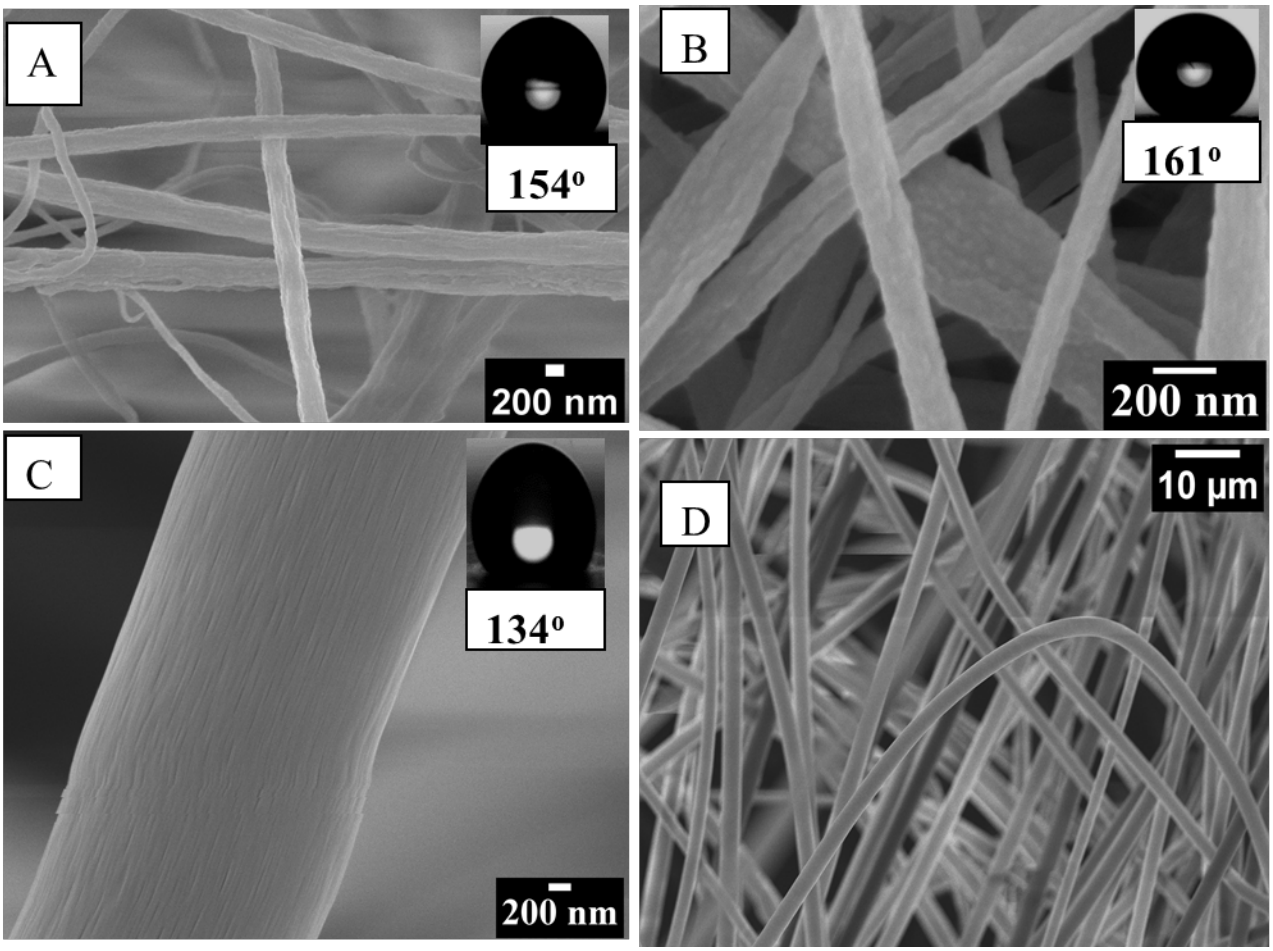

Figure 3. Scanning electronic microscope (SEM) image of PS-G-SiF with contact angle 154° (A), PS-MWCNT-SiF with contact angle 161° (B) fibers and PS fibers with contact angle 134° (C and D).

3. Results and discussion

Mechanically-robust multifunctional nanocomposite membranes were developed to separate oil and water mixture based on the following premises: (1) superhydrophobicity can improve the separation of oil from the mixture of oil and water; (2) rational design of dispersion materials in the matrix can enhance the mechanical properties of the composite membrane. Thus, graphene and MWCNT were selected as dispersion materials for the composites since they have

high Young's modulus, which would enhance the stiffness of the composites through rational design, and a strong hydrophobic property.

Superhydrophobic electrospun fiber membranes were successfully obtained by controlling the ratio of polystyrene with either carbon nanotubes or graphene nanoflakes. The roughness of the electrospuns resulted in the superhydrophobicity as the ratio between the polystyrene and either CNT or graphene was optimized (**Figure 3 A and B**). The highest water contact angle obtained for pure PS fibres reached 134° when the concentration of PS was 20% (**Figure 3C and D**). It can be easily seen that surface roughness of both PS composite fibres, PS-G-SiF (graphene and fluorinated silane) (**Figure 3A**) or PS-MWCNT-SiF (MWCNT and fluorinated silane) (**Figure 3B**), is larger than that of pure PS fibres. The high surface roughness led to superhydrophobicity. The water contact angles obtained for both PS-G-SiF and PS-MWCNT-SiF fibres are 154° and 161°, respectively. The concentration of PS was selected from 5% to 20 % in terms of the formation of the fibres. At the same time, the concentration of both graphene and MWCNT in these two different composites was still determined by the formation of fibres in the electrospinning process. The average diameters of the composite fibres (either PS-MWCNT-SiF or PS-G-SiF) were relatively reduced. Furthermore, the average diameter of the PS fibers was around 2 μm, whereas the mean diameters for the PS-G-SiF fibers and PS-MCNT-SiF were about 200-300 nm and around 100-200 nm, respectively. The super-hydrophobicity of the composites was ascribed to the surface roughness and air-trap in the composite fibres (Shao et al., 2021; Wang et al., 2011).

The formation of two different types of composites was confirmed by experimental analytic tools. The XPS technique confirmed the chemical modification of both MWCNT and graphene with 1*H*,1*H*,2*H*,2*H*-Perfluorodecyltriethoxysilane (PFDTES). Figure 4 and Figure S2 show the XPS analysis of PS-MWCNT-SiF fibers. The compositions of four major elements are listed in **Table 1**. These results were compared with the corresponding theoretical values. According to the XPS results, the concentration of F, C and Si atoms was lower than that in the 1*H*,1*H*,2*H*,2*H*-Perfluorodecyltriethoxysilane (PFDTES) molecule. The reason for this is that the molecular weight of the compound increased after PFDTES was chemically bonded to the MWCNT. The concentration of oxygen was increased because more oxygen atoms from PFDTES were added to the new compound. Furthermore, the curve of C^{1s} was deconvoluted into different Gaussian lines (**Figure 4**). The C^{1s} peaks at 290-293 eV and at 294 eV in the modified MWCNT were assigned to the C-F_2 bond and C-F_3 peak, respectively. The second highest peak at 286 eV was due to the C-O bonds. A broad peak from 284 to 288 eV was assigned to Si−C−O and C-O bonds. The C=O peaks appeared at 289 eV (**Figure 4a**). The two peaks of CF_2 and CF_3 from 690 to 695 eV originated from the C-F bonds in the PFDTES (**Figure 4b**). The peaks of Si between 101 and 106 eV were assigned as the Si-O bonds (103-104 eV), and Si-O-C (104-105 eV) (**Figure 4c**). The peaks of O^{1s} between 533 and 534 eV are C=O and C-O bonds, respectively. The data of Si−C−O and C-O-Si from the peak of C and Si indicates the successful modification of MWCNT with PFDTES (**Figure 4d**) (Oke et al., 2019; Okpalugo et al., 2005; Pacheco et al., 2015).

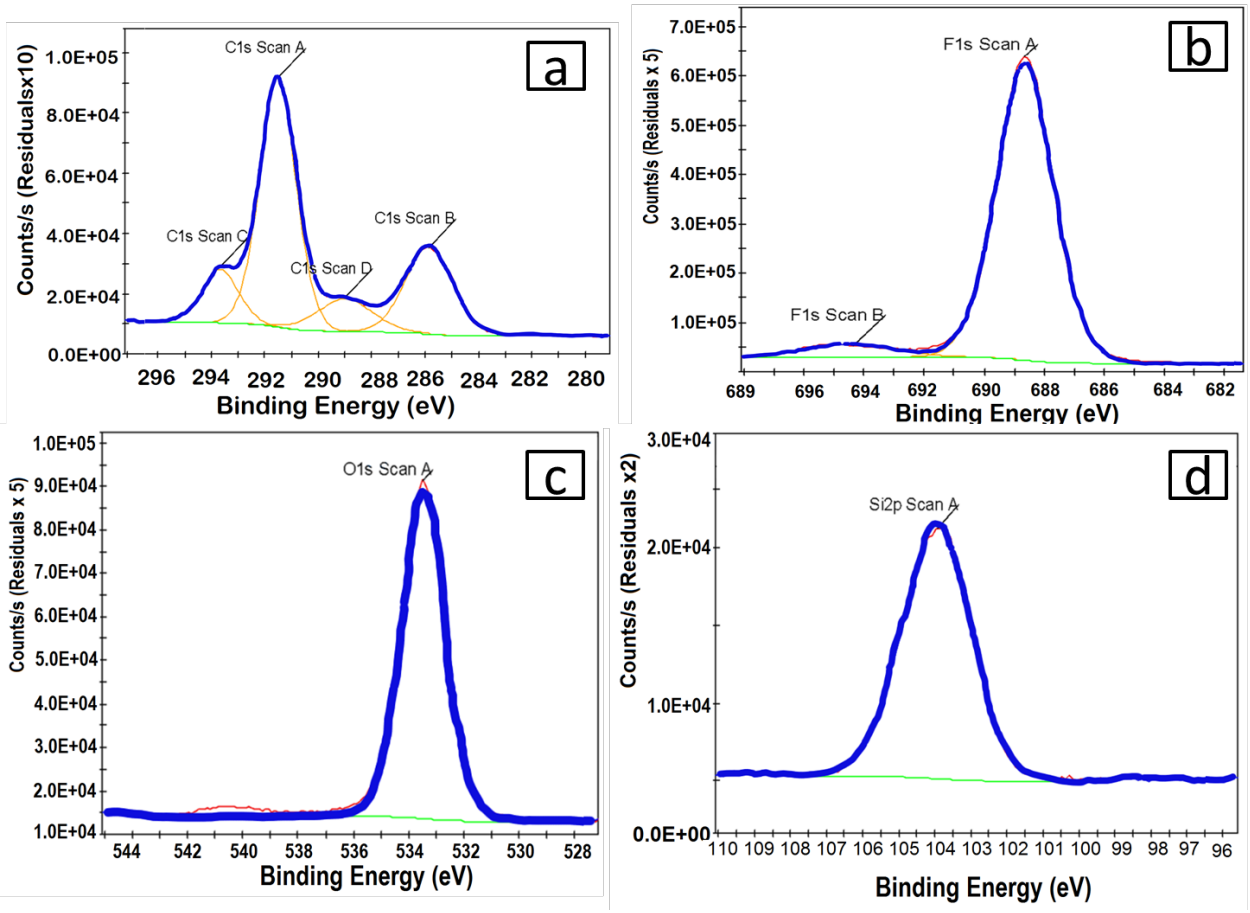

Figure 4. De-convoluted high resolution XPS data curves for C^{1s} (a), F^{1s} (b), O^{1s} (c) and Si^{sp} (d).

To confirm the presence of either MWCNT or graphene nanoflakes in the PS composite fibres, Raman spectroscopy technique was further applied to investigate their composition. The Raman spectra of PS-MWCNT-SiF and PS-G-SiF fibres are shown in **Figure S3**. The D-peaks, which are disordered bands of carbon structure due to the sp^2 hybridization, appeared in the range of 1300 – 1400 cm^{-1}. The sharp G band peaks between 1500 – 1600 cm^{-1}, indicating the stretching and vibration in the lattice of carbon atoms in the MWCNT and graphene nanoflakes, are shown in the 1579 cm^{-1} for MWCNT and 1599 cm^{-1} for graphene. Interestingly, the split peaks between 1579 and 1599 cm^{-1} indicated the G- vibrations along with the circumferential (G^-) and vibrations along the direction of the nanotube axis for functionalized CNT (G^+). In the curve of PS-MWCNT-SiF, G^- was stronger than G^+, which indicates that the circumferential vibrations are in abundance. On the contrary, G^- peak is weaker than G^+, showing that no obvious circumferential vibrations present in the graphene (Hussain et al., 2017; Rebelo et al., 2016).

The 2D peaks, which are the most significant peaks for the graphitic carbon material (especially asymmetric shaped multilayer structure), appeared at 2600 cm^{-1} – 2900 cm^{-1}. The two separated peaks for MWCNT at 2694 cm^{-1} and 2905 cm^{-1} originated from the strain or stress of CNT by PS along the circumferential and along the direction of the nanotube axis. Nevertheless,

the peak at 2694 cm^{-1} is higher than the peak at 2905 cm^{-1}, proving the strain along the circumferential direction. As far as the graphene in PS-G-SiF fibers was concerned, two nearly merged peaks were revealed at 2605 and 2904 cm^{-1}. The peak at 2904 cm^{-1} was much higher than the peak at 2605 cm^{-1}, indicating that the strain or stress by PS occurred only on the flat sheet. The 2D peaks of graphene shifted to a higher wavenumber since CNT could be the hydrophobic interaction between graphene sheet and polymer, which caused higher energy demand for strain or stress to occur (Bagotia et al., 2019; Chipara et al., 2013; Singh et al., 2011).

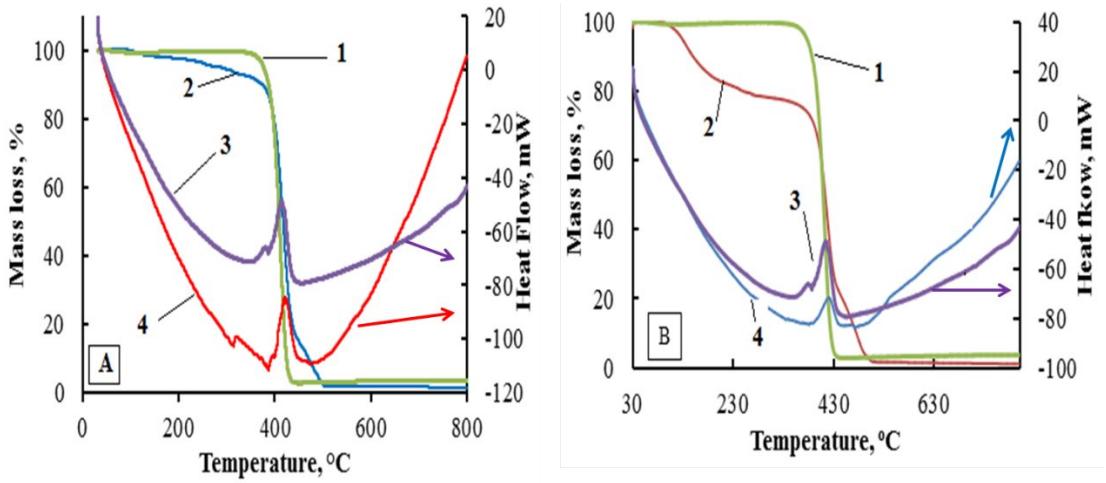

Figure 5. (A) Thermogravimetric analysis (TGA) and differential scanning calorimetry (DSC) analysis of the polymer composites for PS (1, 3) and PS-MWCNT-SiF fibres (2, 4); (B) for PS (1,3) and PS-G-SiFs fibers (2, 4).

Figure S4 shows the FTIR spectra of PS-MWCNT-SiF and PS-G-SiF, where the spectrum of PS is given as reference. The functional groups for PS fiber spectra are recorded below: 3059 cm^{-1} and 3025 cm^{-1} for the aromatic C – H stretch, 2920 cm^{-1} for the tertiary C – H stretch, 2854 cm^{-1} for CH_2 symmetric stretch, C – C ring stretching at 1601 cm^{-1} and 1492 cm^{-1}, CH_2 bending peaks at 1452 cm^{-1}, 1371 cm^{-1} peaks for C – H symmetrical bending, 1068 and 1028 cm^{-1} for inplane CH deformation, 754 cm^{-1} out of plane C – H bending and 695 cm^{-1} C – C out of plane ring deformation. The characteristic peaks for Si-O-C and Si-O-Si were recorded at 1154 cm^{-1} from the fluorosilane molecules. The peaks at 903 and 1021 cm^{-1} were ascribed to MWCNT and graphene in the polymer composites and the peak at 1068 cm^{-1} corresponded to the C-O- bonds in the functionalized MWCNT in the mixture (MacOssay et al., 2012; Shi et al., 2021).

The composition and structures of polymer composites were investigated by thermogravimetric analysis (TGA) and differential scanning calorimeter (DSC) techniques (Simultaneous Thermal Analyzer (STA) 6000). In TGA analysis, 3% mass loss occurred until 370 °C due to the evaporation of solvent (DMF). 91% loss of mass in the range from 409 °C to 426 °C was ascribed to the degradation of PS fibers (**Figure 5A and Figure 5B**, **curve 1**). These losses were also proved by DSC analysis (**Figure 5A and Figure 5B**, **curve 3**). Two exothermic curves were recorded in DSC: at 411 °C for the melting and 429 °C for degradation. Unlike the PS fiber, the PS-MWCNT-SiF fibers showed different thermal properties. In the thermal analysis of PS-MWCNT-SiF, nearly 17% mass loss was determined before melting starts, the degradation

temperature started at 470 °C (**Figure 5A curve 2**). The increase in melting and degradation temperatures can be explained by heat conductivity of MWCNT that increases the thermal resistance of the nanocomposites. In the DSC curves, the glass transition temperature (313 °C) and melting temperature (385 °C) are clearly observed, respectively. However, in the degradation region (**Figure 5A curve 4**), the observed broad peak proves the aforementioned assumptions that the degradation of the PS-MWCNT-SiF fibers needs a higher temperature comparing to PS fibers. Interestingly, it was found that the mass loss of the PS-G-SiF fibers started faster than PS-MWCNT-SiF fibers. This is a clear evidence that in the PS-MWCNT-SiF fibers, the chemical bonding (covalent bonding) between functionalized MWCNT and Si needs more temperature to be broken. But in the PS-G-SiF fibers, there might be only weak dipole-π attractions between graphene and fluorosilane molecules. Hence, the bonds are easily broken at low temperatures. Thus, at 370 °C, 22% mass loss occurred due to the loss of fluorosilicon molecules, but the degradation temperature started at 480 °C (**Figure 5B, curve 2**). This may be due to the fact that the heat conductivity of graphene is a little higher than the thermal conductivity of MWCNT. The melting and degradation phenomena of PS-G-SiF fibres in DSC curves also prove the thermal analysis **Figure 5B**, **curve 4**) (Shi et al., 2021).

To improve stiffness of the polystyrene fibre, two different materials with high Young's

Table 2. Young's Modulus results obtained by two different approaches.

#	Mixture	Young's modulus by tensile test	Young's modulus by AFM
1	PS	7.0547 MPa	10.62 MPa
2	PS + 0.25% Graphene	9.8921 MPa	13.12 MPa
3	PS + 0.25%MCNTS	27.157 MPa	26.95 MPa

Modulus were selected to add the polystyrene matrix membrane as dispersion phase materials. The length of the dispersion phase materials is critical to improve the stiffness of the polystyrene composite materials. The two candidate materials as dispersion phase materials are MWCNT and graphene nanoflakes. Furthermore, the dimension of graphene nanoflake is much smaller than its critical length, the MWCNT is vice versa. As described in the Experimental section, the AFM was applied to measure the average Young's Modulus of the three different types of Polystyrene fibers which are PS, PS-MWCNT-SiF, and PS-G-SiF fibers. Measurement of nanomechanical properties by AFM are already explained in **Figure S1**. Height and Young's modulus of samples are illustrated in **Figure 6**. The Young's Modulus measurement by AFM indicates the steep increase in Young's modulus with the addition of graphene and carbon nanotubes. However, the addition of carbon nanotubes reflects a steeper peak of Young's modulus as compared to graphene. The PS-G-SiF fiber has an average Young's modulus of 14.2 MPa, while PS-MWCNT-SiF has about 27 MPa. The Young's modulus for PS:G (polymer composite with Graphene nanoflakes) and PS:C (polymer composite with MWCNT) is 1.3 and 2.5 times respectively larger than PS. A tensile test meter was applied to measure the Young's modulus for the above samples in parallel. The results

(**Table 2**) show that the addition of both graphene and MWCNT into PS matrix membrane increased the Young's modulus of the PS composites. The Young's modulus was increased from 7.05 MPa to 9.89 MPa with the addition of 0.25% of graphene. However, the same amount of CNT increased Young's modulus almost 4 times.

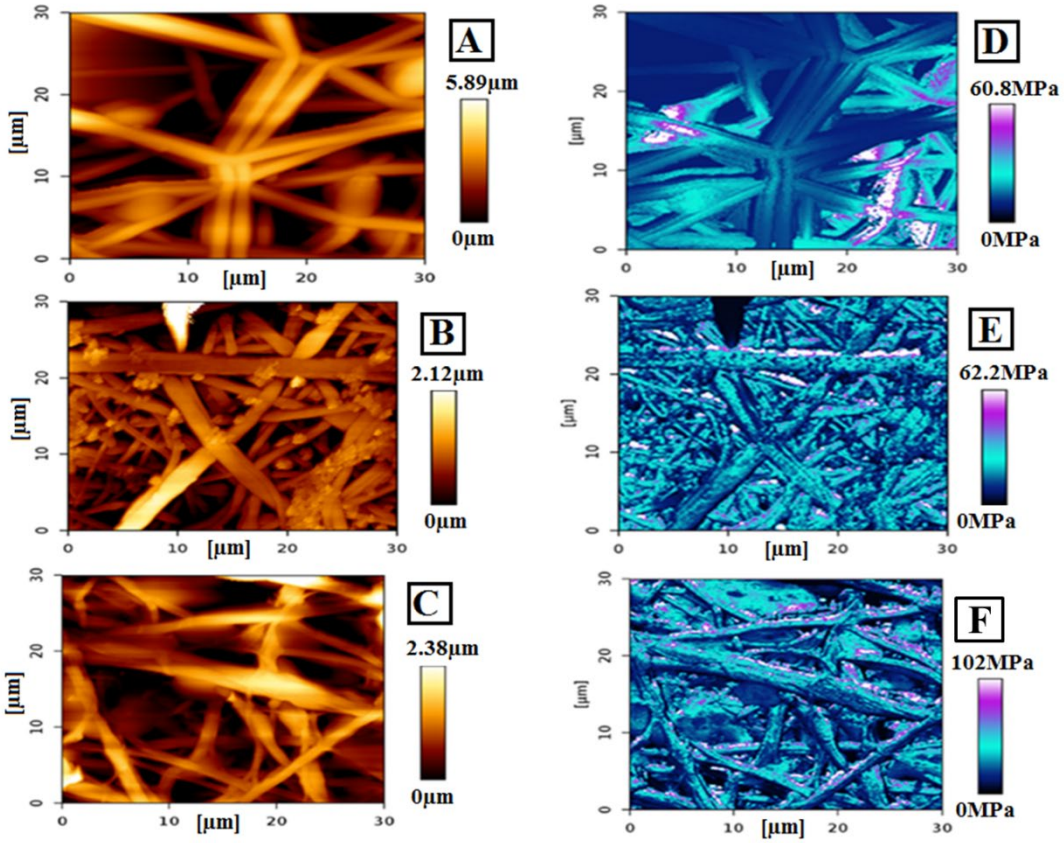

Figure 6. Topographic reconstruction of polystyrene before and after treatment with composite material. (A-C) Height profiles, (A) Polystyrene, (B) Polystyrene with graphene, (C) Polystyrene with carbon nano tube. (D-F) Young's modulus, (D) Polystyrene, (E) Polystyrene with graphene, (F) Polystyrene with carbon nanotube.

To explain the above results or why the PS-MWCNT-SiF composite fiber shows the highest Young's Modulus, the critical lengths of the dispersed phase materials (carbon nanotubes or graphene nanoflakes) for PS-MWCNT-SiF and PS-G-SiF composites were respectively evaluated since both were made of carbon. It is obvious that the length of MWCNT is close to millimetre range, which is much longer or million times longer than that of the graphene nanoflakes (diameter in nanoscale). At the same time, it is longer than it's critical length required into the polymer fibers (**Figure 7 Left**), however, graphene nanoflake is vice versa or less than critical length of graphene in the PS-G-SiF fiber (**Figure 7 Right**). Furthermore, addition of long CNTs enhanced Young's modulus of polymer composites due to very high tensile strength of CNTs. As shown in **Figure 7**, while the length of CNT in the composite is much longer than the critical length, the mechanical strength of the composite has been enhanced dramatically as shown in **Figure 7Left)** and close to the stiffness of the dispersed phase materials. In the case of the

composite of PS-G-SiF, the length of graphene nanoflakes is smaller than its critical length (**Figure 7Right**). Thus the stiffness of the composite is much lower than the stiffness of the dispersed phase materials (graphene nanoflakes).

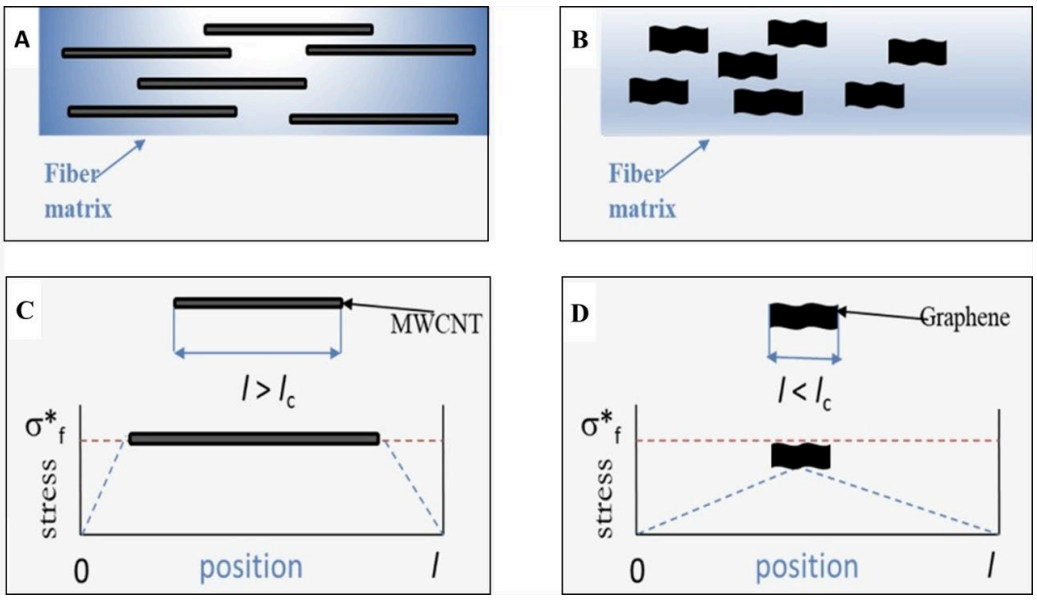

Figure 7. Scheme illustration of lengths of MWCNTs (A) and Graphene nanoflakes (B) vs their critical lengths (C and D) to show the relationship between stress of composite and stress of the dispersed materials.

The above obtained superhydrophobic PS-MWCNT-SiF and PS-G-SiF membranes were tested for the separation of oil/water mixture based on the hypothesis that superhydrophobic property can improve the oil/water separation efficiency. In this test, 100 mL mixture of cyclohexane and water at equal 1:1 ratio was poured into a separation flask. Water was colored in red with food dye to be more visible. While the mixture was poured into the separation flask, first cyclohexane touched the surface of the membrane and small amount of cyclohexane passed through it. Then due to low density of cyclohexane (0.779 g/mL) relative to the water, it went up immediately and floated on the top of water (**Figure 8-a**). Thus, water layer blocked the cyclohexane from passing through the membrane. Thereafter, we stirred the mixture of water and cyclohexane to make cyclohexane contact the membrane surface. Thus, cyclohexane was extracted from water.

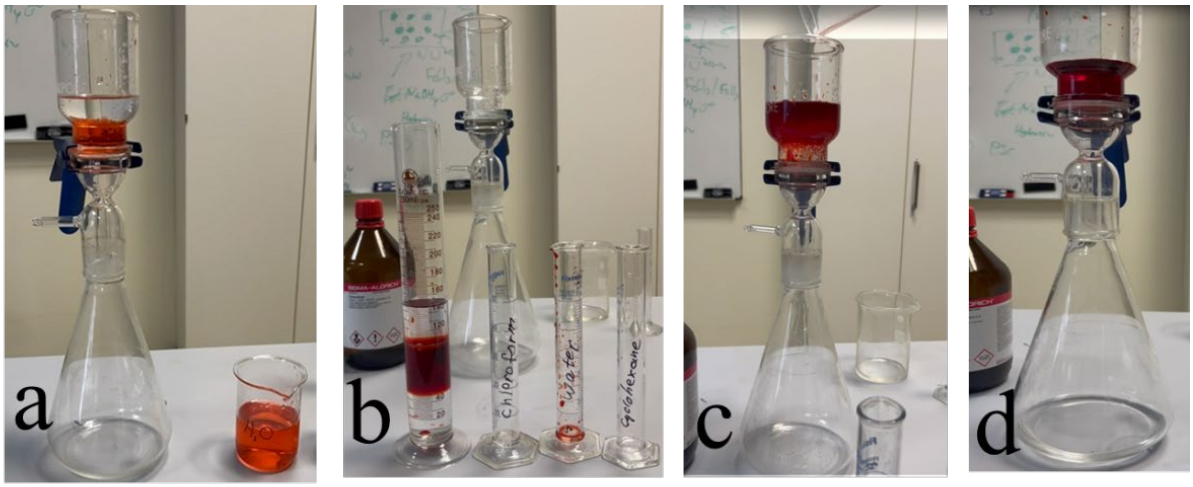

Figure 8. Oil/water separation procedure. Red food colouring was added to water to distinguish from clear oil solution. (a) Mixture of cyclohexane and water; (b) Mixture of cyclohexane-water-chloroform; (c) Before the separation oil from water; (d) After separation.

In the second experiment, equal volume (50 mL each) of chloroform, water and cyclohexane were transferred into a graduated cylinder to form three layers based on the density difference of solvents (**Figure 8-b**). As shown in the **Figure 8-c**, the mixture was poured in the separation flask, the oil phase was permeated through the membrane and dropped into the flask, no single red drop (water) was revealed in the flask. After 135 seconds, only water layer (colored in red) was left. The water and oil phases were measured after separation. The remaining water was 50 mL (100 % separation) and oil phase was 98 mL, the 2 mL was probably absorbed on the membrane. Details of the experiment can be seen from the video (**Figure S5**). The membranes exhibited a high flux of 693 L $m^{-2}h^{-1}$. This result indicated that superhydrophobic membrane can separate the water/oil mixture efficiently, which can be extended to industrial fields including oil leakage in ocean/sea/river and purification of oil for car feed.

4. Conclusion

In this research, the superhydrophobic nanocomposite fibers, PS-MWCNT-SiF and PS-G-SiF, have been developed to test for oil/water separation. The modification of MWCNT and graphene with fluorosilane molecules improved the hydrophobic and mechanical properties of the above nanocomposite fibers. Furthermore, dispersed phases called, i.e., graphene and MWCNT were modified with fluorosilane molecules. These molecules functioned as crosslinker and the cross-linked fillers lead to the robust superhydrophobic composite membranes. These membranes improved the water and oil separation performance. Goniometer was applied to confirm the superhydrophobicity of the membranes. Spectroscopic tools including FTIR, Raman, and XPS confirmed the inclusion and modification of dispersed phase materials, i.e., MWCNT and graphene. The stiffness of the nanocomposite fibers was evaluated by nanoindentation (AFM) and

a tensile tester. A nanocomposite model was developed to explain the highest stiffness of PS-MWCNT-SiF. The membrane showed excellent performance for oil-water separation. This result can be potentially extended for the deployment in the industrial field.

Acknowledgment:

This work was supported by the Ministry of Education and Science of the Republic of Kazakhstan under the project No. AP09258910 "Multifunctional Desulfurization Polymer Nanocomposites". The authors would like to thank the Deanship of Scientific Research at Umm Al-Qura University for supporting this work by Grant Code: (22UQU4320141DSR06).

References

Asmatulu, R., Ceylan, M., Nuraje, N., 2011. Study of superhydrophobic electrospun nanocomposite fibers for energy systems. Langmuir 27, 504–507. https://doi.org/10.1021/la103661c

Bagotia, N., Choudhary, V., Sharma, D.K., 2019. Synergistic effect of graphene/multiwalled carbon nanotube hybrid fillers on mechanical, electrical and EMI shielding properties of polycarbonate/ethylene methyl acrylate nanocomposites, Composites Part B: Engineering. Elsevier Ltd. https://doi.org/10.1016/j.compositesb.2018.10.009

Beyer, J., Trannum, H.C., Bakke, T., Hodson, P. V., Collier, T.K., 2016. Environmental effects of the Deepwater Horizon oil spill: A review. Mar. Pollut. Bull. 110, 28–51. https://doi.org/10.1016/j.marpolbul.2016.06.027

Chipara, D.M., MacOssay, J., Ybarra, A.V.R., Chipara, A.C., Eubanks, T.M., Chipara, M., 2013. Raman spectroscopy of polystyrene nanofibers - Multiwalled carbon nanotubes composites. Appl. Surf. Sci. 275, 23–27. https://doi.org/10.1016/j.apsusc.2013.01.116

Cirer-Costa, J.C., 2015. Tourism and its hypersensitivity to oil spills. Mar. Pollut. Bull. 91, 65–72. https://doi.org/10.1016/j.marpolbul.2014.12.027

Datsyuk, V., Kalyva, M., Papagelis, K., Parthenios, J., Tasis, D., Siokou, A., Kallitsis, I., Galiotis, C., 2008. Chemical oxidation of multiwalled carbon nanotubes. Carbon N. Y. 46, 833–840. https://doi.org/10.1016/j.carbon.2008.02.012

de Oliveira Estevo, M., Lopes, P.F.M., de Oliveira Júnior, J.G.C., Junqueira, A.B., de Oliveira Santos, A.P., da Silva Lima, J.A., Malhado, A.C.M., Ladle, R.J., Campos-Silva, J.V., 2021. Immediate social and economic impacts of a major oil spill on Brazilian coastal fishing communities. Mar. Pollut. Bull. 164. https://doi.org/10.1016/j.marpolbul.2021.111984

Egan, A.L., Chilvers, B.L., Cassells, S., 2021. Does size matter? The direct economic costs associated with the MV Rena oil spill. Mar. Pollut. Bull. 173, 112978. https://doi.org/10.1016/j.marpolbul.2021.112978

Hong, S.K., Bae, S., Jeon, H., Kim, M., Cho, S.J., Lim, G., 2018. An underwater superoleophobic nanofibrous cellulosic membrane for oil/water separation with high separation flux and high chemical stability. Nanoscale 10, 3037–3045. https://doi.org/10.1039/c7nr08199e

Huang, M., Si, Y., Tang, X., Zhu, Z., Ding, B., Liu, L., Zheng, G., Luo, W., Yu, J., 2013. Gravity driven separation of emulsified oil-water mixtures utilizing in situ polymerized superhydrophobic and superoleophilic nanofibrous membranes. J. Mater. Chem. A 1,

14071–14074. https://doi.org/10.1039/c3ta13385k
Hussain, M., Naeem, M.N., Shahzad, A., He, M., 2017. Vibrational behavior of single-walled carbon nanotubes based on cylindrical shell model using wave propagation approach. AIP Adv. 7. https://doi.org/10.1063/1.4979112
Ihsanullah, 2019. Carbon nanotube membranes for water purification: Developments, challenges, and prospects for the future. Sep. Purif. Technol. 209, 307–337. https://doi.org/10.1016/j.seppur.2018.07.043
International Tanker Owners Pollution Federation, London, UK, 2021, 2010. Oil tanker spill statistics 2010.
Kang, M., Jung, R., Kim, H.S., Jin, H.J., 2008. Preparation of superhydrophobic polystyrene membranes by electrospinning. Colloids Surfaces A Physicochem. Eng. Asp. 313–314, 411–414. https://doi.org/10.1016/j.colsurfa.2007.04.122
Lei, L., Zhang, Q., Shi, S., Zhu, S., 2017. Highly Porous Poly(high internal phase emulsion) Membranes with "open-Cell" Structure and CO2-Switchable Wettability Used for Controlled Oil/Water Separation. Langmuir 33, 11936–11944. https://doi.org/10.1021/acs.langmuir.7b02539
MacOssay, J., Ybarra, A.V.R., Arjamend, F.A., Cantu, T., Eubanks, T.M., Chipara, M., López-Cuéllar, E., Mohamed-Noriega, N., 2012. Electrospun polystyrene-multiwalled carbon nanotubes: Imaging, thermal and spectroscopic characterization. Des. Monomers Polym. 15, 197–205. https://doi.org/10.1163/156855511X615065
Nelson, J.R., Grubesic, T.H., Sim, L., Rose, K., 2018. A geospatial evaluation of oil spill impact potential on coastal tourism in the Gulf of Mexico. Comput. Environ. Urban Syst. 68, 26–36. https://doi.org/10.1016/j.compenvurbsys.2017.10.001
Nuraje, N., Khan, W.S., Lei, Y., Ceylan, M., Asmatulu, R., 2013. Superhydrophobic electrospun nanofibers. J. Mater. Chem. A 1, 1929–1946. https://doi.org/10.1039/c2ta00189f
Oke, J.A., Idisi, D.O., Sarma, S., Moloi, S.J., Ray, S.C., Chen, K.H., Ghosh, A., Shelke, A., Pong, W.F., 2019. Electronic, Electrical, and Magnetic Behavioral Change of SiO2-NP-Decorated MWCNTs. ACS Omega. https://doi.org/10.1021/acsomega.9b01958
Okpalugo, T.I.T., Papakonstantinou, P., Murphy, H., McLaughlin, J., Brown, N.M.D., 2005. High resolution XPS characterization of chemical functionalised MWCNTs and SWCNTs. Carbon N. Y. 43, 153–161. https://doi.org/10.1016/j.carbon.2004.08.033
Pacheco, F.G., Cotta, A.A.C., Gorgulho, H.F., Santos, A.P., Macedo, W.A.A., Furtado, C.A., 2015. Comparative temporal analysis of multiwalled carbon nanotube oxidation reactions: Evaluating chemical modifications on true nanotube surface. Appl. Surf. Sci. 357, 1015–1023. https://doi.org/10.1016/j.apsusc.2015.09.054
Peters, B.D., Stebar, R.F., 1976. Water-gasoline fuels-their effect on spark ignition engine emissions and performance. SAE Tech. Pap. 85, 1832–1853. https://doi.org/10.4271/760547
Rebelo, S.L.H., Guedes, A., Szefczyk, M.E., Pereira, A.M., Araújo, J.P., Freire, C., 2016. Progress in the Raman spectra analysis of covalently functionalized multiwalled carbon nanotubes: Unraveling disorder in graphitic materials. Phys. Chem. Chem. Phys. 18, 12784–12796. https://doi.org/10.1039/c5cp06519d
Ritchie, R.K., Kulawic, D., 1970. Identification and Determination of Freezing-Point-Depressant Anti-Icing Additives in Hydrocarbon Fuels by Infrared Spectrometry. Anal. Chem. 42, 1080–1084. https://doi.org/10.1021/ac60291a030
Rodrigues, B.V.M., Silva, A.S., Melo, G.F.S., Vasconscellos, L.M.R., Marciano, F.R., Lobo,

A.O., 2016. Influence of low contents of superhydrophilic MWCNT on the properties and cell viability of electrospun poly (butylene adipate-co-terephthalate) fibers. Mater. Sci. Eng. C 59, 782–791. https://doi.org/10.1016/j.msec.2015.10.075

Shao, L., Cheng, X.Q., Jiao, Y., Sun, Z., Yang, X., Cheng, Z., Bai, Q., Zhang, Y., Wang, K., 2021. Constructing scalable superhydrophobic membranes for ultrafast water-oil separation. ACS Nano 15, 3500–3508. https://doi.org/10.1021/acsnano.1c00158

Shi, C., Qian, X., Jing, J., Che, H., 2021. Functionalized CNTs with DOPO and Silicon Containing Agents: Effective Reinforcer for Thermal and Flame Retardant Properties of Polystyrene Nanocomposites. Front. Chem. 8, 1–9. https://doi.org/10.3389/fchem.2020.627642

Singh, B.P., Samal, S., Nayak, S., Majhi, S.M., Besra, L., Bhattacharjee, S., 2011. The production of a multi-walled carbon nanotube/hexamethylene diisocyanate nanocomposite coating on copper by electrophoretic deposition. Surf. Coatings Technol. 206, 1319–1326. https://doi.org/10.1016/j.surfcoat.2011.08.054

Singh, E., Hlaing, P., Dibble, R.W., 2020. Investigating water injection in single-cylinder gasoline spark-ignited engines at fixed speed. Energy and Fuels 34, 16636–16653. https://doi.org/10.1021/acs.energyfuels.0c03057

Sun, H., Xu, Y., Zhou, Y., Gao, W., Zhao, H., Wang, W., 2017. Preparation of superhydrophobic nanocomposite fiber membranes by electrospinning poly(vinylidene fluoride)/silane coupling agent modified SiO2 nanoparticles. J. Appl. Polym. Sci. 134, 1–8. https://doi.org/10.1002/app.44501

Wang, S., Li, Yapeng, Fei, X., Sun, M., Zhang, C., Li, Yaoxian, Yang, Q., Hong, X., 2011. Preparation of a durable superhydrophobic membrane by electrospinning poly (vinylidene fluoride) (PVDF) mixed with epoxy-siloxane modified SiO2 nanoparticles: A possible route to superhydrophobic surfaces with low water sliding angle and high water contac. J. Colloid Interface Sci. 359, 380–388. https://doi.org/10.1016/j.jcis.2011.04.004

Wiley, J., 2013. Liu , Y ., MacFadyen , A ., Ji , Z . G ., & Weisberg , R . H . . Monitoring and modeling the deepwater 195.

Wu, J., Li, H., Lai, X., Chen, Z., Zeng, X., 2019. Superhydrophobic Polydimethylsiloxane@Multiwalled Carbon Nanotubes Membrane for Effective Water-in-Oil Emulsions Separation and Quick Deicing. Ind. Eng. Chem. Res. 58, 8791–8799. https://doi.org/10.1021/acs.iecr.9b00994

Zeiger, C., Kumberg, J., Vüllers, F., Worgull, M., Hölscher, H., Kavalenka, M.N., 2017. Selective filtration of oil/water mixtures with bioinspired porous membranes. RSC Adv. 7, 32806–32811. https://doi.org/10.1039/c7ra05385a